

## Large-scale flow driven by turbulently generated internal gravity waves

P. Léard <sup>\*</sup>, L. Marguillan, T. Raymond , M. Rouby , and M. Le Bars   
CNRS, Aix Marseille Université, Centrale Marseille, IRPHE, Marseille 13013, France



(Received 24 March 2021; accepted 30 June 2021; published 2 August 2021)

The generation of large-scale flows by stochastically excited internal gravity waves remains largely unexplored despite numerous applications in geophysical and astrophysical contexts. Here, we investigate this problem experimentally in a cylindrical annulus geometry. Our working fluid is made of two layers. In the top, fresh water layer, turbulence is generated by 12 jets with an oscillating flow rate. Those turbulent fluctuations impinge the interface with the bottom, linearly stratified, salt water layer, where they excite internal gravity waves which propagate, damp viscously, and generate a mean azimuthal flow. The jet structure, wave spectra, and mean-flow properties are addressed using particle image velocimetry. Our measurements validate quantitatively the transfer of momentum from the waves to the mean flow through the wave associated Reynolds stress, as previously validated for a monochromatic forcing. In addition, wave energy decays through time, likely because of the mixing at the interface between the two layers, and the driven mean flow accordingly decreases and eventually vanishes. This has up to now prevented the observation of quasibiennial-oscillation-like reversals in our system.

DOI: [10.1103/PhysRevFluids.6.084801](https://doi.org/10.1103/PhysRevFluids.6.084801)

### I. INTRODUCTION

The emergence of large-scale dynamics from small-scale fluctuations is a quite studied topic in geophysics and astrophysics; see, e.g., the formation of zonal jets on gaseous planets [1,2] or the zonal wind oscillations observed on Earth's, Saturn's and Jupiter's atmospheres [3–5]. In those cases, the large-scale dynamics is driven by momentum exchanges with the small-scale fluctuations. To investigate some aspects of planet stratospheres and star radiative layers, the forcing induced by internal gravity waves is especially relevant to study. A single internal gravity wave propagating through a fluid can force a mean flow [6–11], similarly to the more known example of acoustic streaming [12]. In addition, internal gravity waves have the specific property of being antidiffusive [13]: they reinforce the mean flow that propagates in the same direction, and accentuate velocity gradients. The most striking manifestation of this process is indubitably the quasibiennial oscillation (QBO) [3], an oscillation of stratospheric zonal winds observed in the Earth's atmosphere, from westward to eastward flow, with a mean period of 28 months.

The QBO mechanism was first theoretically developed by Holton and Lindzen [14,15]. A model focusing only on forcing by internal gravity waves was later introduced and validated experimentally by Plumb and McEwan [16,17]. This model is based on a monochromatic, standing forcing, with two internal gravity waves propagating in the same vertical direction, but with opposite horizontal velocities. Theory predictions accord remarkably well with experimental results, which were recently extended to longer durations and to a larger parameter space [18]. Yet, the forcing in this theory and its experimental realization is idealized and cannot compare to the stochastic forcing observed in the Earth's atmosphere [19]. Two-dimensional direct numerical simulations

---

<sup>\*</sup>Present address: ETHZ, D-ERDW, GEG, Zurich, Switzerland; pierre.leard@erdw.ethz.ch

have recently shown that mean-flow reversals can also emerge from convectively generated internal gravity waves [20]. In addition, a stochastic one-dimensional model expanding upon the original Plumb's model [16] has shown that, surprisingly, increasing stochasticity in the forcing reinforces the regime of regular oscillations [21]. But to the best of our knowledge, experiments have until now stayed in the monochromatic, standing, laminar limit [8,10,17,18].

To complement the observational, numerical, and theoretical evidences of the possibility of large-scale flow emergence from stochastically generated internal gravity waves, we experimentally tackle this topic in a setup close to the original Plumb's QBO experiment [17] and present our results in this paper. Section II introduces the setup and the theoretical model. Section III then presents and discusses the experimental results. Lastly, Sec. IV summarizes our main conclusions and lists possible improvements for future works.

## II. MODEL, SETUP, AND METHODS

### A. Theoretical model for internal gravity wave streaming

The theoretical model initiated by [16] is briefly introduced here to provide the basic knowledge for understanding the underlying physical mechanisms as well as the experimental geometry and results. Interested readers should refer to [18,22] for more details.

We consider a two-dimensional ( $\mathbf{e}_x, \mathbf{e}_z$ ) Cartesian domain, periodic along the horizontal  $x$  axis, and filled with a stably stratified fluid of constant buoyancy frequency  $N$ , with gravity pointing downward  $\mathbf{g} = -g\mathbf{e}_z$ . We decompose the velocity field as  $\mathbf{u} = \bar{\mathbf{u}} + \mathbf{u}'$ , where  $\bar{\mathbf{u}} = (\bar{u}, 0)$  is the horizontally averaged flow and  $\mathbf{u}' = (u', w')$  are the small-scale fluctuations, coming from internal gravity waves in our framework. The time evolution of the horizontal mean-flow  $\bar{u}$  is rigorously described by

$$\partial_t \bar{u} - \nu \partial_{zz} \bar{u} = -\partial_z (\overline{u'w'}). \quad (1)$$

The right-hand term in Eq. (1) is the  $z$  derivative of the Reynolds stress associated with the waves. It illustrates that the attenuation of the wave flux  $F = \overline{u'w'}$  with respect to height forces the horizontal mean flow. The expression for the wave flux  $F$  can be analytically derived for a single plane wave as done thoroughly in [22], including an extensive description of the different underlying assumptions. Simply reproducing here the final expression from [10] for illustration purposes relevant to our setup, we have

$$F(z) = F(0) \exp\left(-\frac{1}{d} \int_0^z \left[ \frac{\alpha}{[1 - \bar{u}(z')/c]^2} + \frac{1 - \alpha}{[1 - \bar{u}(z')/c]^4} \right] dz'\right), \quad (2)$$

where

$$d = \frac{\alpha k_x c^4}{\nu N^3} \quad (3)$$

is the wave attenuation length in the weak dissipation limit [23] and in the absence of mean flow, and  $\alpha = \frac{\nu N^2}{\nu N^2 + \gamma c^2}$  quantifies the relative influence of bulk viscosity  $\nu$  in the wave damping process, which also includes wall friction denoted by  $\gamma$  (see also [18]).  $c$  stands for the wave horizontal velocity  $c = \omega/k_x$ , with  $\omega$  the wave frequency ( $0 \leq \omega \leq N$ ) and  $k_x$  its horizontal wave number, and  $F(0)$  is the wave flux at the boundary of the stratified layer where the wave is generated. The main feature of the forcing (2) is that because of the corrective factors in the integral, the effective wave attenuation length is shorter when the wave characteristic velocity  $c$  is oriented in the same direction as the mean-flow  $\bar{u}$ , which is then more strongly reinforced by the momentum transfer from the damped wave. For example, if the mean flow in the stratified layer is positive, waves with positive  $c$  velocity attenuate within a shorter distance than waves with negative  $c$  velocity, which propagate further in the domain.

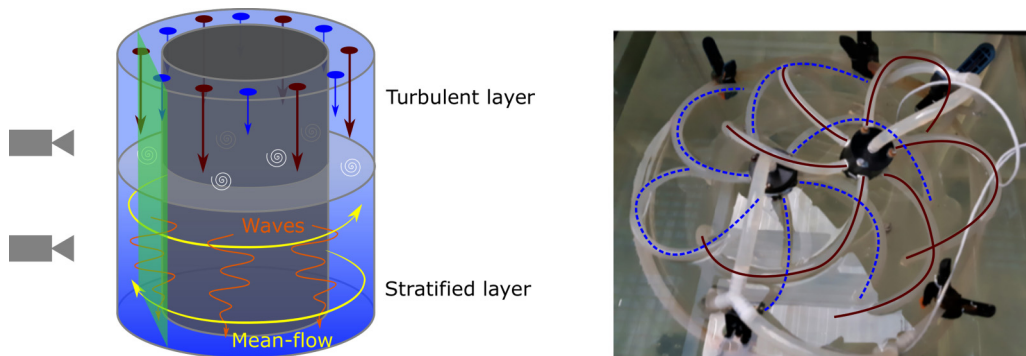


FIG. 1. Left: Schematic of the cylindrical annulus geometry. Turbulence in the top layer is generated by 12 jets emerging from the red and blue holes. Waves are generated at the interface between the turbulent and stratified layers and an azimuthal mean flow is observed. The positions of the green laser sheet and cameras for particle image velocimetry (PIV) are also pictured. The figure is not to scale. Right: Top photograph of the setup and injection plate. The flow from the two pumps is divided into 12 pipes directed to the nozzle exits at the top of the tank. The dotted blue (respectively, thick red) pipes are connected to the blue (respectively, red) holes at the top of the tank in the left panel.

### B. Tank description

The working tank has a concentric double cylinder geometry (see left panel of Fig. 1) and is reminiscent of the tank used in the celebrated experiment of Plumb and McEwan [17], later extended by Semin *et al.* [18]. Neglecting the curvature of the double cylinder as well as radial motions, this geometry is equivalent to the two-dimensional (2D) Cartesian periodic model described above, with the azimuthal  $\mathbf{e}_\theta$  direction being equivalent to the horizontal periodic  $\mathbf{e}_x$  direction of the model. The cylinders are 60 cm high and have diameters of  $d_1 = 20$  cm (respectively,  $d_2 = 40$  cm) for the inner (respectively, outer) cylinder. For practical reasons (e.g., optical distortions), the cylinders are placed into a rectangular tank whose dimensions are  $50 \times 50 \times 75$  cm<sup>3</sup>. All the different volumes (inside the inner cylinder, the working region between the two cylinders, and outside the outer cylinder) are connected at the top and bottom by small holes that allow water to circulate freely.

A depth of 45 cm from the bottom of the tank is filled with a linear gradient of salty water using the double-bucket technique [24]. Above this stratified layer stands a 25-cm-high layer of homogeneous fresh water. A circular plate with 12 holes regularly distributed azimuthally is located 10 cm below the free surface. One of every two holes is connected to a first pump, and the remaining six holes are connected to a second pump, as pictured in the right panel of Fig. 1. The pumps take water from the top of the tank, outside the outer cylinder, in order to avoid any perturbation on the dynamics of interest.

This configuration generates a turbulent layer through the interaction of the 12 jets. The pump flow rates are modulated sinusoidally, with a period of  $T = 20$  s and a phase lag between the two pumps of  $\varphi = 180^\circ$ , hence a typical forcing wavelength  $\lambda = 16$  cm (the holes are equally spaced on a  $d = 30$ -cm-diameter circle). These parameters allow us to impose a large-scale modulation in the turbulent layer which has similar properties as the harmonic forcing in the experiment of [18], in terms of period and wave number. Thus, the forcing for the internal gravity waves consists in a large-scale modulation that forces waves at an imposed and controlled frequency, superimposed to smaller and faster fluctuations resulting from the turbulent cascade of energy from the jets. Doing so, we reproduce the forcing of [17,18] which succeeded in driving a large-scale, reversing flow, and we investigate the additional effects of small-scale turbulence.

After filling the tank, the density is measured every 5 cm within the stratified layer using an electronic densimeter Anton Paar DMA 35. The density profile shown in Fig. 2 is as expected

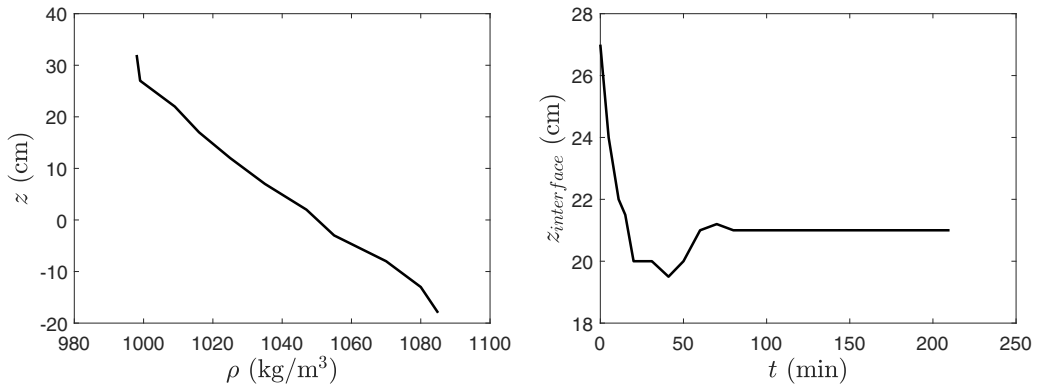


FIG. 2. Left: Density profile taken before an experiment. In our convention,  $z = 0$  is the bottom of the stratified layer camera field, so the interface is initially located at  $z = 27$  cm, with a homogeneous layer of fresh water above and a constant  $N = 0.21$  Hz stratified layer below. Right: Interface position over time during an experiment. At  $t = 45$  min, the refilling process is started.

linear, with a constant buoyancy frequency

$$N = \frac{1}{2\pi} \sqrt{\frac{-g}{\rho_0} \frac{\partial \rho}{\partial z}} = 0.21 \text{ Hz.} \quad (4)$$

In Fig. 2, as in all the following, the coordinate origin ( $x = 0, z = 0$ ) is located at the bottom left corner of the field visualized by our stratified layer camera (see next section). This origin is located 18 cm above the tank bottom, hence the interface between the stratified and homogeneous layers is located initially at  $z = 27$  cm, and the jets emerge from  $z = 42$  cm.

The major issue of our setup is the mixing occurring at the interface. The turbulence in the upper layer entrains and mixes salty fluid at the top of the stratified layer, resulting in a slow depth decrease over time (see, e.g., [25]). This is quite problematic since wave-driven flows emerge over similar long timescales, and both effects can significantly interact. To avoid any height variation of the stratified layer, salty fluid is constantly poured at the bottom of the tank during the experiment using the double-bucket technique, following the original idea of Semin *et al.* [18]. An imposed flow rate of about  $0.45 \text{ L min}^{-1}$  balances the mixing rate at the interface, so that the interface stays at the same location over time. The corresponding typical vertical velocity is about  $3 \times 10^{-5} \text{ m s}^{-1}$ , which remains small compared to any other relevant velocity in the system. Fresh water is also pumped out of the tank at the top to keep the total volume constant. With this process, we manage to maintain a constant depth for the interface, as displayed in the right panel of Fig. 2. We see that the interface position initially reaches lower and lower location, until the refilling process starts at time  $t = 45$  min: the interface then slightly rises and finally stabilizes for  $t > 60$  min at  $z = 21$  cm.

### C. Measurements

To quantify the flow in the tank, we perform particle image velocimetry (PIV). The tank is seeded with silver-coated particles of diameter  $10 \mu\text{m}$  and density  $\rho_p = 1040 \text{ kg m}^{-3}$ . The tank is illuminated with a 532-nm, 1-W continuous laser. The laser plane is vertical and tangent to the virtual cylinder of diameter  $(d_1 + d_2)/2 = 30 \text{ cm}$ , i.e., it is located in the middle of the gap between the two cylinders, as pictured in the left panel of Fig. 1. Because of the very different amplitudes of the turbulent and stratified flows, two cameras are used to measure the velocity. A Nikon D5500 films the turbulent layer at 60 fps with a resolution of  $720 \times 1280$  pixels over a  $11 \times 20 \text{ cm}^2$  domain. A Point Grey camera films the stratified layer at 2 fps with a resolution of  $2048 \times 2448$  pixels over a  $20 \times 23 \text{ cm}^2$  domain. Acquired images are processed with DPIVSoft2010 [26] with  $32 \times 32$

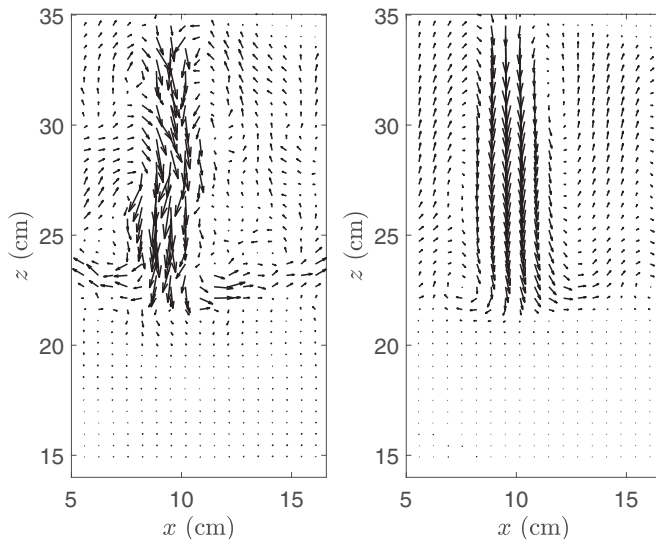


FIG. 3. Left: Instantaneous velocity field in the turbulent layer. One jet is present in the camera view field. Right: Time-averaged signal over a 2-min acquisition time.

pixel interrogation areas and 50% overlapping. Entrainment of salty fluid at the interface blurs the acquired images and the PIV algorithm cannot compute the corresponding velocity vectors close to the interface. The velocities at the exit of the jets and down to  $\sim 5$  cm are also not accessible because of too large vertical velocities relative to the selected frame rate.

### III. RESULTS

#### A. Jet structure

This paper thoroughly describes a set of experiments where the flow rate  $Q$  oscillates between 1 and 2  $\text{L min}^{-1}$ . Maximum recorded velocities at about 5 cm below the injection holes coherently reach  $15 \text{ cm s}^{-1}$ . With holes diameter  $d = 1 \text{ cm}$ , a lower bound estimate of the jet Reynolds number is  $\text{Re} \sim 1500$  and the jets are weakly turbulent. An instantaneous field is displayed in the left panel of Fig. 3 and shows the structure of the jet at a given time. The flow is directed downward and is deflected horizontally due to the stratified layer at  $z \sim 21 \text{ cm}$ . In the stratified layer ( $z < 21 \text{ cm}$ ), the fluid seems motionless: velocities are actually much smaller and are studied using the second camera, as described in the next section. In the jet, small vortices are also observed, being transported by the downward jet flow. The right panel shows a time-averaged field over a 2-min window. The time-averaged jet shares similar characteristics with the instantaneous one. Only the small vortices are filtered out.

It is important to remember that the jet is not continuously blowing at a constant flow rate, but it is modulated by a sinusoidal shape as illustrated in the left panel of Fig. 4. The vertical velocity observed at a single point is shown in the right panel of Fig. 4. The imposed period  $T = 20 \text{ s}$  can be noticed, with vertical velocities oscillating between  $\sim 0 \text{ cm s}^{-1}$  and  $\sim -6 \text{ cm s}^{-1}$ . Small positive velocities are sometimes reached and are due to the influence of the adjacent jets. When the flow rate of the jet within the camera frame is at its minimum, the two adjacent jets are at their maximum flow rate and create an upward return flow at the location chosen to plot the velocity signal shown here.

The time-averaged velocity field is shown in the right panel of Fig. 3. From that mean profile, we extract the vertical velocity at several heights and we plot these horizontal profiles in Fig. 5. Going deeper into the tank, the jet velocity decreases and its radius increases, always maintaining

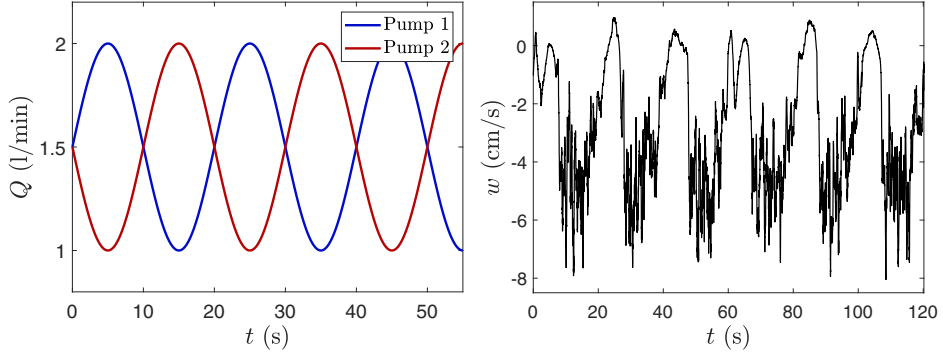


FIG. 4. Left: Flow rate of the two pumps due to the imposed sinusoidal modulation. Right: Observed vertical velocity at a single point located at  $x = 10$  cm and  $z = 27$  cm (see Fig. 3). One can notice the imposed period  $T = 20$  s.

its mostly Gaussian shape. Another feature of this figure is that the  $x$  position of the maximum velocity slightly shifts to the right as the jet goes deeper into the layer, as highlighted by the red line. When the jet gets closer to the interface, the maximum position shifts back to its initial position. Yet, one can also observe that the Gaussian profile of the jet is still skewed towards positive  $x$ . We explain these effects by a large-scale circulation taking place in the turbulent layer. This large-scale flow is present in every single experiment performed, and is always directed in the same direction, i.e., in the positive  $x$  direction. Despite our efforts and careful checking of the horizontality of our injection plate and perpendicularity of all the nozzles, we did not manage to remove this large-scale contribution from our turbulent layer. Yet, its amplitude ( $\sim 0.1$  cm s $^{-1}$ ) is relatively small compared to the vertical velocities involved (a few cm s $^{-1}$ ). The influence of this large-scale circulation is only to slightly deviate the jets towards positive  $x$  at intermediate depths, as pictured in Fig. 5.

Figure 6 shows the vertically and time-averaged power spectral density (PSD) with respect to the horizontal wave number  $k_x$  (left panel) and to the frequency  $f$  (right panel). The PSD with

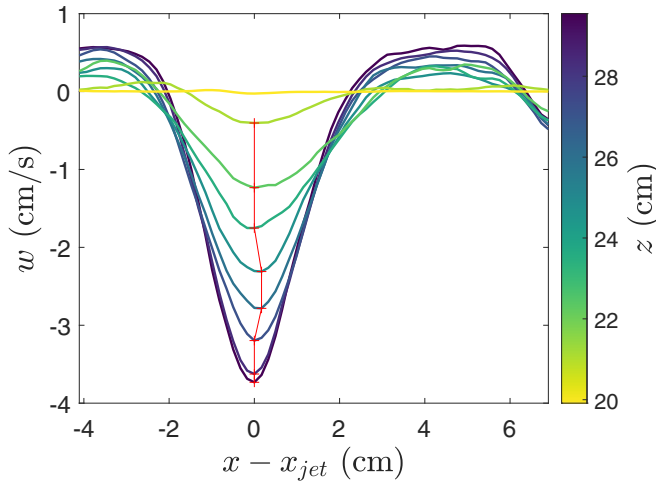


FIG. 5. Horizontal profiles of vertical velocities taken from the time-averaged velocity field displayed in Fig. 3. The colors indicate the  $z$  position, with dark purple located at the top of the jet and yellow located just below the interface.  $x_{jet}$  is the center of the injection hole. The red line shows the location of maximum velocity for each height.

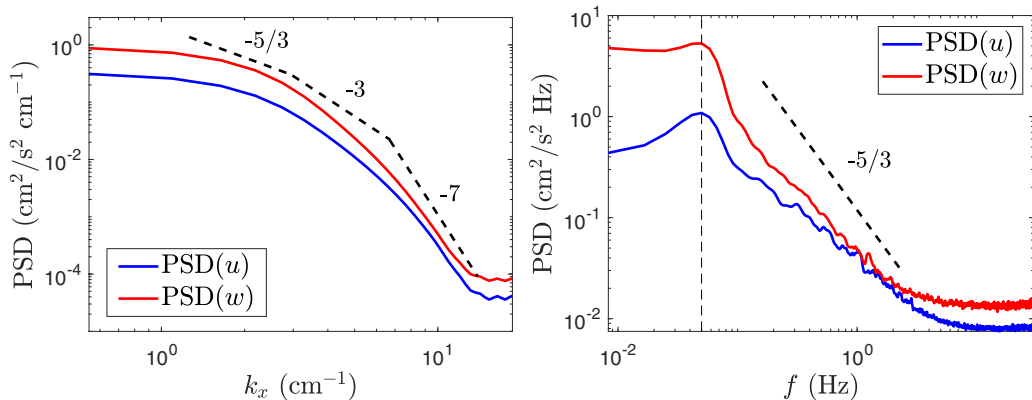


FIG. 6. Left: Power spectral density of the horizontal (blue) and vertical (red) velocities as a function of the horizontal wave number  $k_x$ . Different slopes characterizing the spectrum for turbulent jets are displayed in a dashed line [27]. Right: Power spectral density of the horizontal (blue) and vertical (red) velocities as a function of the frequency  $f$ . The dashed line shows the  $-5/3$  slope for reference. The vertical dashed line indicates the frequency of the forcing  $f = 1/T = 5 \times 10^{-2}$  Hz.

respect to  $k_x$  is computed from PSDs at each time and each depth in the turbulent layer and then vertically and time averaged. The mean PSD shares similar slopes with turbulent jets described in [27], respectively corresponding to an energy cascade dominated by inertial transfers at small  $k_x$  (slope  $-5/3$ ) and by viscous effects at large  $k_x$  (slope  $-7$ ), separated by a transition zone with a slope  $-3$  tentatively related by [27] to local two-dimensional effects. The averaged PSD with respect to  $f$  peaks at  $f = 5 \times 10^{-2}$  Hz, which corresponds to the  $T = 20$  s period imposed to the jets. The energy then decreases for  $f > 5 \times 10^{-2}$  Hz with a slope close to  $-5/3$ , presumably corresponding to the advection of the inertial range of the turbulent spectrum by the jet mean flow.

## B. Stratified layer

Images taken from the second, slow frame rate camera, allow us to describe the internal gravity wave field and the mean-flow properties.

### 1. Internal gravity waves

The left panel of Fig. 7 shows an instantaneous velocity field. Maximum velocities in the stratified layer are approximately  $3 \text{ mm s}^{-1}$ , i.e., 50 times smaller than the maximum velocities in the upper layer. Horizontal and vertical motions observed in Fig. 7 are the signature of the turbulently generated internal gravity waves. Above  $z = 20$  cm, the motions of the turbulent layer are too fast for the camera acquisition rate and result in false vectors computed by the PIV algorithm. A temporal signal of the vertical velocity  $w$  taken at  $x = 10$  cm and  $z = 16.5$  cm is shown in the top right panel. The oscillating behavior of  $w$  is obviously noticeable. However, the forcing period  $T = 20$  s does not particularly stand out. This suggests that the waves are generated over a large range of frequencies, as expected. The bottom right panel shows the time evolution of the vertical velocity  $w$  along the  $x$  axis at  $z = 16.5$  cm. Oscillations are observed along the whole  $x$  axis and are identified as internal gravity waves by comparing the observed signal to the theoretical polarization relation in Fig. 8. The forcing period  $T = 20$  s is more noticeable here, but it is still superimposed with shorter period waves.

To describe more precisely the wave pattern, we compute horizontally averaged power spectra density of the horizontal and vertical velocities at the height  $z = 16.5$  cm. PSDs are computed at each  $x$  location from a 1-h signal and then horizontally averaged. The top left panel of Fig. 8 shows

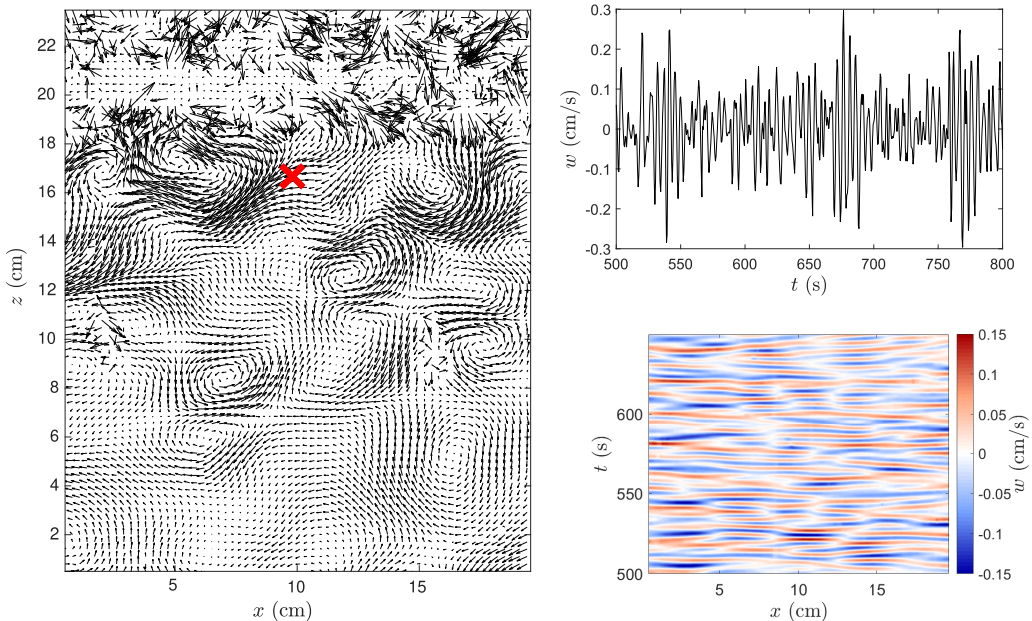


FIG. 7. Left: Instantaneous field in the stratified layer. Top right: 5-min vertical velocity signal at the location  $x = 10$  cm,  $z = 16.5$  cm, pictured by the red cross in the left panel. Bottom right: Spatiotemporal diagram showing the vertical velocity  $w$  along the  $x$  axis at  $z = 16.5$  cm from a 150-s signal.

the PSD of the horizontal velocity  $u$ . A significant amount of energy is present at low frequencies. This is the signature of a large-scale, horizontal flow which will be described later. The energy drops at  $f \sim 10^{-3}$  Hz. Then the energy increases again from  $f = 10^{-2}$  Hz to  $f \sim 10^{-1}$  Hz, with a marked cutoff at  $f = 2.1 \times 10^{-1}$  Hz, corresponding to the buoyancy frequency  $N$ . High-energy peaks are also observed. The first one at  $f = 5 \times 10^{-2}$  Hz corresponds to the forcing frequency  $1/T$ . Following peaks are harmonics of the forcing frequency. The PSD of the vertical velocity  $w$  is displayed in the top right panel of Fig. 8 and shares with the PSD of  $u$  the increasing energy and marked peaks starting at  $f = 1/T$ , and the cutoff at  $f = 2.1 \times 10^{-1}$  Hz. It is, however, significantly less energetic at low frequencies  $f < 10^{-3}$  Hz. The remaining low velocity at low frequency is related to the continuous refilling process. The bottom panel of Fig. 8 shows the ratio  $\text{PSD}(u)/\text{PSD}(w)$  in black and the polarization relation of linear internal gravity waves  $(u/w)^2 = (N/\omega)^2 - 1$  in red. We see a good agreement between the two curves in the range  $1/T \leq f \leq N$ , showing that oscillating motions at these frequencies are essentially internal gravity waves, contrary to motions at lower frequencies. This is further confirmed by the good quantitative agreement between the measured PSDs and the PSDs derived from the other velocity component combined with the polarization relation, shown as gray dashed lines in the top panels of Fig. 8.

The  $z$  dependence of the wave energy has been investigated. Figure 9 shows the horizontally averaged PSD of the horizontal velocity  $u$  (top panel) and vertical velocity  $w$  (bottom panel), computed at each height: it confirms the main conclusions above. A lot of energy is present at low frequencies for the horizontal velocity, over the whole tank depth. The forcing frequency and harmonics are visible along the whole depth for both velocity components, and the energy is cut off at  $N = 2.1 \times 10^{-1}$  Hz. Almost no energy is seen at any height for  $2 \times 10^{-3}$  Hz  $< f < 8 \times 10^{-3}$  Hz, and only a small amount of energy is then seen up to the excitation frequency  $1/T$ . The velocity signal is thus composed of a slow, mean horizontal flow, superimposed to internal waves with frequency  $1/T \leq f \leq N$ .

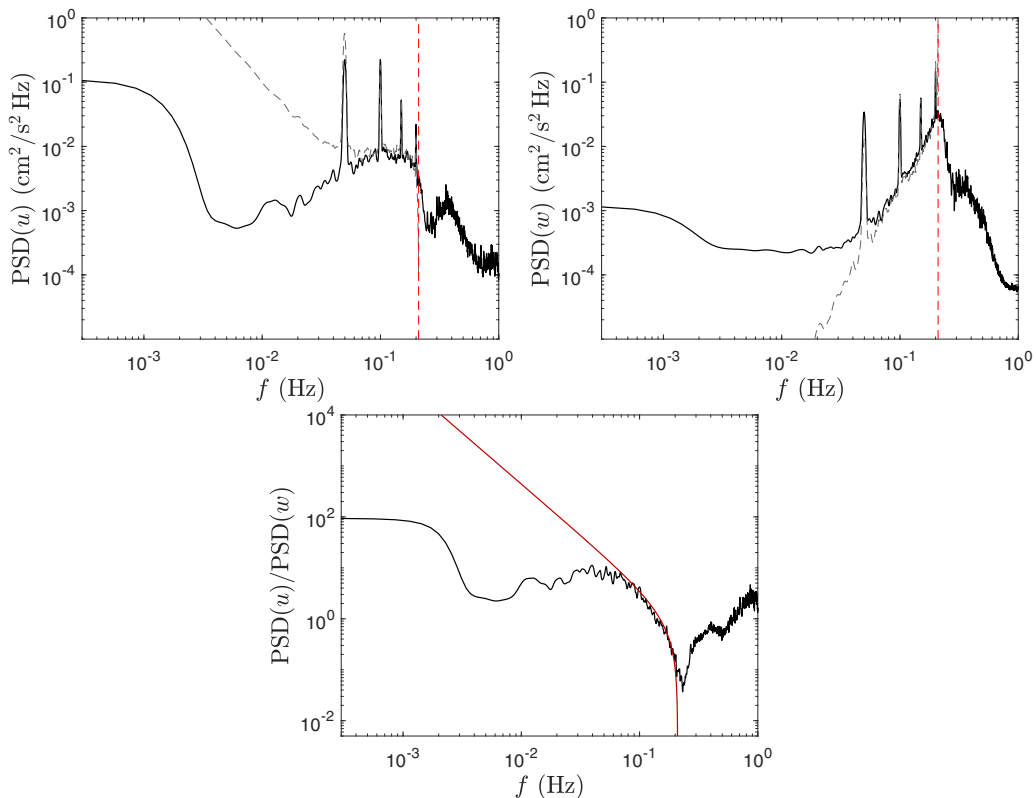


FIG. 8. Left: PSD of the horizontal velocity  $u$  computed at  $z = 16.5$  cm for each horizontal location and then horizontally averaged. The red dashed line shows the buoyancy frequency  $N = 0.21$  Hz and the gray dashed curve shows the theoretical spectra computed from the polarization relation and the experimental spectra of  $w$ :  $\text{PSD}(u_{\text{th}}) = \text{PSD}(w)[(N/\omega)^2 - 1]$ . Right: Same for the vertical velocity  $w$ . Bottom: The ratio  $\text{PSD}(u)/\text{PSD}(w)$  is plotted in black. The polarization relation of internal gravity waves  $(u/w)^2 = (N/\omega)^2 - 1$  is plotted in red. All PSDs are computed between  $t = 300$  s and  $t = 3500$  s.

One could have expected a stronger frequency dependence of the wave attenuation with depth, as predicted from Eq. (3) which indicates an attenuation depth scaling in frequency with a power 4, and as seen, for example, in [23] for a convective excitation. Indeed, the dispersion relation links the pulsation of the wave with its angle of propagation  $\omega/N = \cos(\theta)$ .  $\theta$  is the angle between gravity and the group velocity direction (perpendicular to the wave vector). For low (respectively, close to  $N$ ) frequency waves,  $\theta \rightarrow \pi/2$  (respectively,  $\theta \rightarrow 0$ ) and therefore the energy propagates almost perpendicular to the gravity, i.e., horizontally (respectively, vertically). Therefore, we expect frequencies close to  $N$  to propagate deeper than frequencies small compared to  $N$ . This dependence of the attenuation on the wave frequency is not clearly visible here and most of the waves seem to reach the bottom of the measurement window. Actually, the attenuation length depends on frequency but also on the horizontal wave number  $k_x$ , and there is no reason to assume that waves at different frequencies have the same  $k_x$  (as opposed to the convective excitation studied in [23]). On the contrary, with a Kolmogorov-like description of the jet turbulence, one would expect  $f \propto k_x^{2/3}$  [28]; from Eq. (3), this would lead to a dependence of the attenuation depth in  $f^{-1/2}$  considering only bulk viscosity. This effect combined with the influence of wall friction explains the rather weak dependency of the attenuation length upon the wave frequency observed in the PSDs presented in Fig. 9. Note also that Eq. (3) is valid for a two-dimensional plane wave in the weak propagation

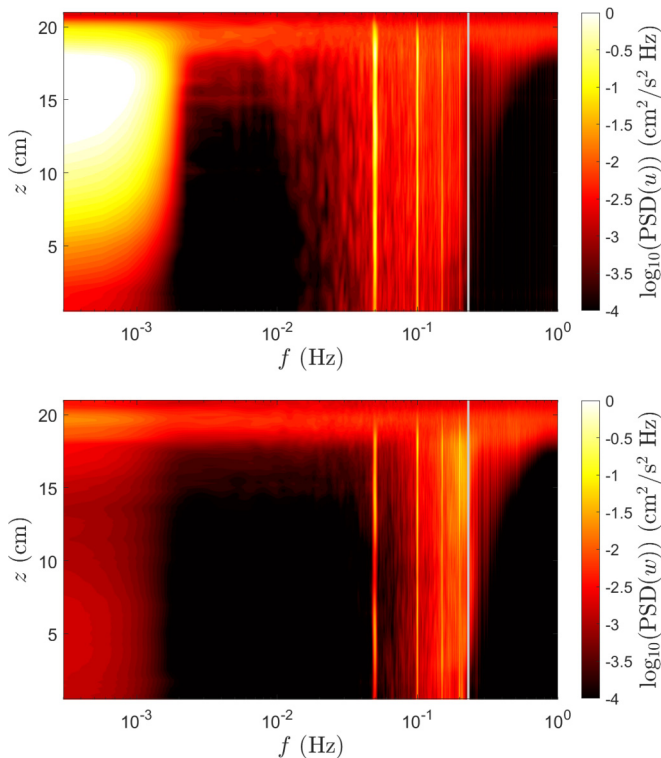


FIG. 9. PSDs of the horizontal velocity  $u$  (top) and of the vertical velocity  $w$  (bottom) with respect to frequency and height. The buoyancy frequency  $N$  is shown by the gray vertical line. The PSDs are computed between  $t = 300$  s and  $t = 3500$  s.

limit only, and hence does not account for the full dissipation (see discussion in [23]) nor for the specific cylindrical shell geometry of our system (see Appendix B of [17]). In any case, the depth profile of the integrated energy for the wave part of the spectrum  $1/T \leq f \leq N$ , shown in Fig. 10, confirms some wave damping with depth, which, as we show in the next paragraph, is at the origin of the measured, horizontal mean flow. Additionally, one can notice the small depth dependency of the signal forced at the main forcing frequency  $1/T$  and its harmonics, which exhibit the presence of nodes and antinodes: we have thus excited global modes of the system, which according to (1) do not contribute significantly to large-scale flow forcing.

## 2. Large-scale flow

We argue that the energy present at low frequencies in the PSD of the horizontal velocity  $u$  (Fig. 9) is the signature of a slowly evolving, horizontal large-scale flow in the stratified layer. Window time averaging over 500 s and horizontally averaging over the whole field-of-view allow us to estimate the horizontal mean-flow  $\bar{u}$ , whose time evolution along the  $z$  axis is plotted in the left panel of figure 11. At early times, only a small negative flow is observed. Quickly, this negative flow expands deeper, and velocities reach a higher magnitude while a positive flow appears just below the interface. This positive velocity layer is 1 cm thick. The negative layer is thicker but does not reach the bottom of the tank. As mentioned before, the interface reaches lower positions with time at early stages, until we start the refilling process (here at  $t \sim 2200$  s); then the interface location stabilizes. Over an hour of observation, the mean flow does not evolve much and stays in the configuration described above, characterized by a strong shear between the two opposite layers. While the thin,

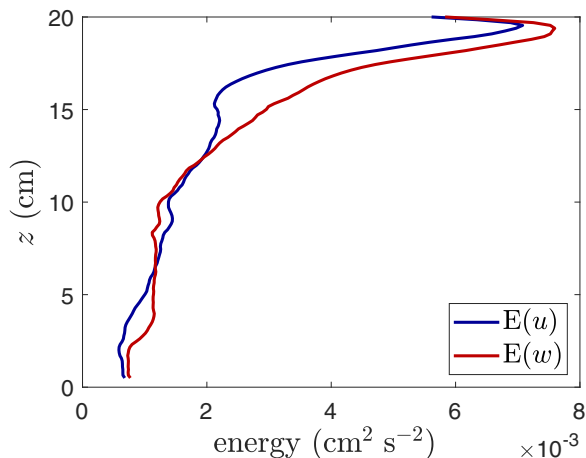


FIG. 10. PSD integrated between the forcing frequency  $1/T$  and the buoyancy frequency  $N$  as a function of depth, for the horizontal (blue) and vertical (red) velocities.

positive velocity layer might be driven by viscous coupling with the observed, residual mean flow in the turbulent layer (see Sec. III A), another driving mechanism is necessary for explaining the strong negative mean flow, which cannot be viscously driven nor related to some passive return flow, since this negative flow is stronger in magnitude and deeper than the positive one. We demonstrate now that it is related to a momentum transfer from the waves, following the mean-flow equation (1).

To quantitatively confirm this, the forcing term  $-\partial_z(\overline{u'w'})$  is computed from our experimental data, and is time averaged over an hour in order to improve the signal-to-noise ratio. Time averaging can be performed here because the mean flow does not evolve much over an hour as seen in the left panel of Fig. 11. The time-averaged wave forcing term profile  $-\partial_z(\overline{u'w'})$  is compared in the right panel of Fig. 11 to the viscous dissipation term of the mean flow  $\nu\partial_{zz}\overline{u}$ . Both equilibrate closely, as expected from Eq. (1) at steady state.

One could also wonder whether the mean flow is somehow connected to our refilling process. However, it turns out that (i) in Fig. 11, the same mean flow appears and persists without any noticeable change before and after the start of the refilling, here at time  $t = 2200$  s, and that (ii)

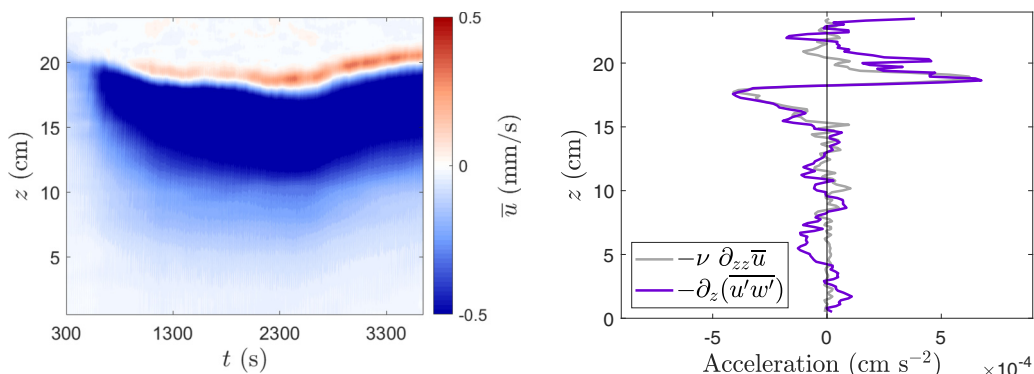


FIG. 11. Left: Horizontal mean-flow  $\overline{u}$  evolution over time. The interface is located at  $z \sim 21$  cm. Right: Vertical, time-averaged profiles of the mean-flow viscous dissipation  $\nu\partial_{zz}\overline{u}$  in gray and of the Reynolds stress forcing term  $-\partial_z(\overline{u'w'})$  in purple.

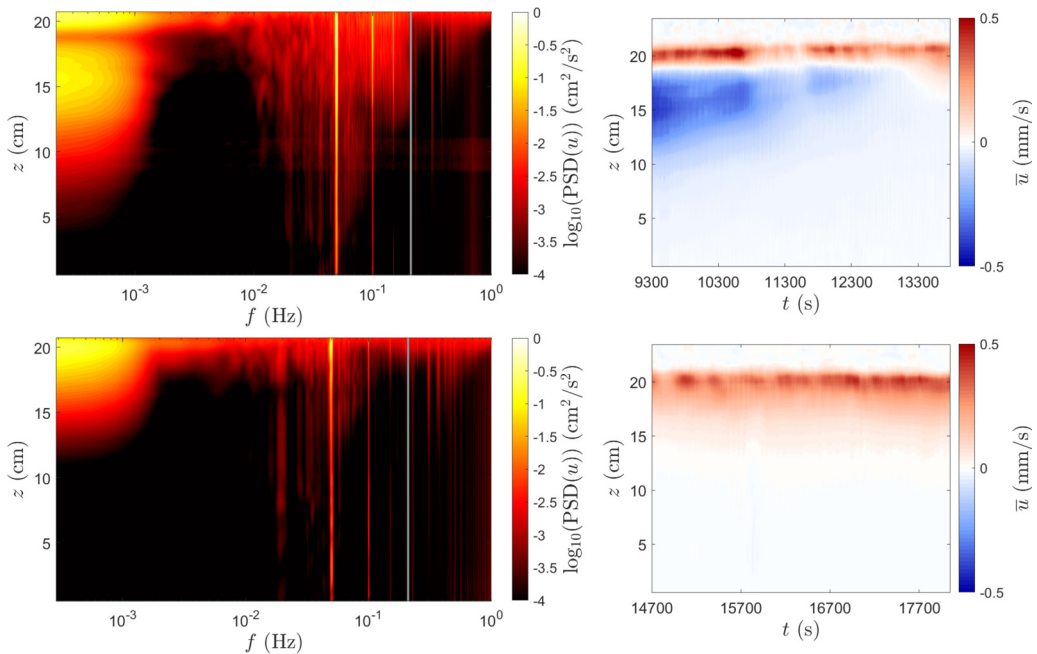


FIG. 12. Top: PSD of the horizontal velocity  $u$  (left) and corresponding time evolution of the horizontal mean-flow  $\bar{u}$  (right) during 1 h continuing the acquisition shown in Figs. 9 and 11. Bottom: PSD of the horizontal velocity  $u$  (left) and corresponding time evolution of the horizontal mean-flow  $\bar{u}$  (right) during 1 h continuing the acquisition shown in the upper panels.

other experiments without using refilling (not shown here) exhibit the same mean flow and temporal evolution.

The long-time evolution of the wave generation and mean-flow dynamics is looked at in Fig. 12, showing the PSD of the horizontal velocity and the time evolution of its horizontal mean  $\bar{u}$  for several time windows for a total experiment time of 5 h. One sees that the wave energy weaker and weaker with time: there is less and less signal in the range  $1/T \leq f \leq N$ . The frequency peaks characterizing the forcing ( $f = 1/T = 5 \times 10^{-2}$  Hz and harmonics) are still highly visible, as well as the low frequency fluctuations associated with the mean flow, yet over a decreasing depth. The mean-flow evolution shows that its positive part close to the interface persists over the whole acquisition time, while the negative part located below slowly vanishes. Eventually, only the positive flow close to the interface remains. We argue that, over time, less and less energy goes into the waves; therefore the negative mean flow which is wave driven, slowly vanishes. The positive part of the mean flow is probably viscously driven by the large-scale circulation observed in the turbulent layer.

To explain the decay in wave energy over time, we advance the issue of entrainment and mixing at the interface. Even if the refilling process allows one to maintain the interface at a fixed location, the entrainment still occurs and creates an increasing density jump between the turbulent and stratified layers. Indeed, in our setup, the jets very quickly rip some fluid away from the top of the stratified layer and mix it within the turbulent layer, without modifying the underlying linear density profile. The density of the turbulent layer increases slightly (the eroded salty water is diluted over the whole top layer), while the density at the top of the stratified layer becomes larger and larger: a step appears and grows in the density profile. Diffusion would tend to erase that step, but for salt, the diffusion is very slow and since the jets continuously entrain salty water at the top of the stratified layer, diffusion does not act fast enough to smooth that profile. The density profile is not discontinuous, but the

transition height remains negligible compared to the turbulent and stratified layer depths. Then, this density jump acts like a barrier: the interface becomes “stiffer,” and less energy is transferred into the waves. Only the main excitation at the forcing frequency  $1/T$  and harmonics persist, yet with decreasing amplitude (see Fig. 12 bottom). But this modal excitation does not force any large-scale flow, since the mode amplitude does not exhibit any depth dependence.

The decrease of excitation efficiency when the interface density jump increases is easily understandable when accounting for the so-called “mechanical oscillator” excitation mechanism [29], where overshooting drafts from the turbulence deflect the interface and trigger internal gravity waves. In the presence of a density jump at the interface, part of the available energy is indeed consumed for compensating the related potential energy, and wave energy accordingly decreases. The decrease of excitation efficiency is less obvious when accounting for direct wave excitation from the Reynolds stress associated to the turbulent fluctuations [28], which seems to be the dominant mechanism when looking at self-consistent, two-layer, convective/stably stratified systems [23]. In this case, it was shown theoretically that the wave excitation is most efficient for very smooth interfaces, which gives an upper bound on the wave flux [28]. However, it was also noticed that precise results depend on the specific shape of the density profile. We are not aware of any systematic experimental or numerical quantification of the energy transfer at the interface between a homogeneous fluid layer and a linearly stratified layer separated by a density jump (see, however, the recent work [30] in the close context of two layers with different stratification): this should be the focus of future work.

#### IV. CONCLUSION

In the present study, we manage to drive, in the stratified layer of our configuration, a horizontal mean flow from turbulently generated internal gravity waves. This mean flow is divided into a thin upper part, confined close to the interface with the turbulent layer and going in the  $+x$  direction, and a deep lower part going in the  $-x$  direction. This  $-x$  directed flow is indubitably due to wave forcing through the vertical derivative of wave Reynolds stress. It slowly vanishes over time, concomitantly with the decrease in excited wave energy, presumably because of the building of a density jump at the interface.

Despite the fact that the observed flow is driven by internal gravity waves, the oscillating feature of the QBO was not recovered in our experiment. Several explanations can be advanced to explain this. First, in all performed experiments, the flow generated in the jet layer was always positive: this highlights a symmetry breaking in our setup, which must nevertheless be very small since it resisted all our careful investigations. Secondly, the decay in wave energy over time takes place over similar timescales as potential reversal period in similar flows (i.e., typically 5000 s in [17]). It is thus possible that the wave forcing becomes too small before it could drive any reversal. Finally, in the theoretical model, the attenuation lengths of the waves are considered small compared to the domain height. This is obviously not the case in our experiment, where some waves rebound at the bottom of the stratified layer, especially those forming modes of high-energy peaks at  $f = 5 \times 10^{-2}$  Hz and harmonics. The mean flow driven by upward propagating, reflected waves might negatively interact with the one driven by downward propagating waves. We briefly addressed this issue in 2D direct numerical simulations with an ad hoc stochastic wave maker, and no-slip conditions at the upper and lower boundaries, using the Dedalus solver [31] (see details in [32]): it turns out that when waves have attenuation length larger than the domain height, a stationary mean flow is indeed observed, as illustrated in the left panel of Fig. 13. The observed mean flow is characterized by two layers with opposite directions and a strong shear located at  $z = 0.025$ , similar to the one observed in Fig. 11. For comparison, the mean flow obtained for a higher domain is shown in the right panel. The oscillating pattern of QBO appears, showing that the vertical extent of the domain is of importance for generating wave-driven flows. This now demands systematic investigation.

To sum up, improving our experimental setup to observe QBO from stochastic forcing necessitates one to (i) increase wave dissipation and (ii) to limit interface mixing. Solutions to access shorter

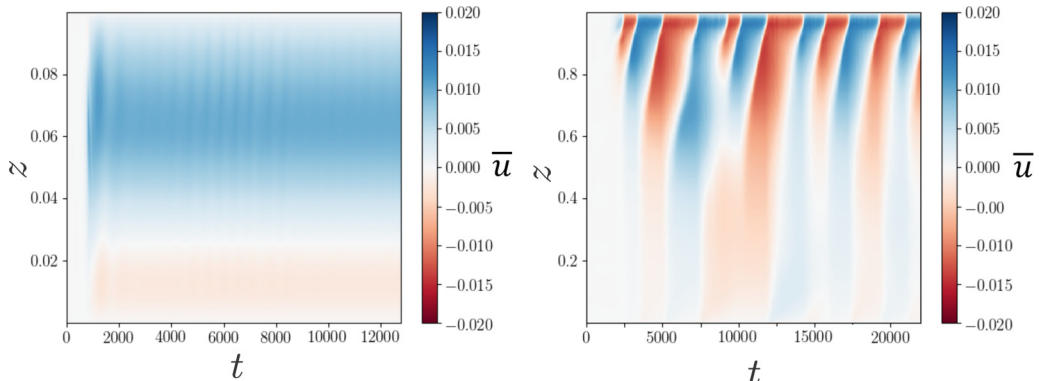


FIG. 13. Left: Horizontal mean-flow  $\bar{u}$  evolution over time in the stratified layer, obtained from 2D direct numerical simulation with an ad hoc stochastic wave maker. The domain height is small compared to the attenuation length of the generated waves. Right: Same for a domain ten times higher. In both cases, the domain is 2D, periodic along the  $x$  axis. The buoyancy frequency is constant. Waves with random phases are forced at the top boundary by setting velocity and buoyancy perturbations.

attenuation lengths are to increase  $N$ , to decrease  $k_x$ , and/or to work with a much higher tank/with a thinner shell/with a larger viscosity fluid (yet remaining turbulent in the upper layer). Solutions to limit mixing imply some type of physical barrier; but those would cancel the wave excitation by turbulent Reynolds stress, which is arguably the dominant mechanism in natural systems [23,28]. Then, jet turbulence may not be the most suited option to stochastically generate internal gravity waves over a long time, and a generating mechanism inspired from [17] but adapted in order to generate polychromatic waves may be a more reliable option for better control of the excitation spectrum.

#### ACKNOWLEDGMENTS

The authors acknowledge funding by the European Research Council under the European Union's Horizon 2020 research and innovation program through Grant No. 681835-FLUDYCO-ERC-2015-CoG.

- 
- [1] P. Irwin, *Giant Planets of Our Solar System: Atmospheres, Composition, and Structure* (Springer Science & Business Media, New York, 2009).
  - [2] A. R. Vasavada and A. P. Showman, Jovian atmospheric dynamics: An update after Galileo and Cassini, *Rep. Prog. Phys.* **68**, 1935 (2005).
  - [3] M. P. Baldwin, L. J. Gray, T. J. Dunkerton, K. Hamilton, P. H. Haynes, W. J. Randel, J. R. Holton, M. J. Alexander, I. Hirota, T. Horinouchi, D. B. A. Jones, J. S. Kinnerson, C. Marquardt, K. Sato, and M. Takahashi, The quasi-biennial oscillation, *Rev. Geophys.* **39**, 179 (2001).
  - [4] C. B. Leovy, A. J. Friedson, and G. S. Orton, The quasiquadrennial oscillation of Jupiter's equatorial stratosphere, *Nature (London)* **354**, 380 (1991).
  - [5] T. Fouchet, S. Guerlet, D. F. Strobel, A. A. Simon-Miller, B. Bézard, and F. M. Flasar, An equatorial oscillation in Saturn's middle atmosphere, *Nature (London)* **453**, 200 (2008).
  - [6] F. P. Bretherton, Momentum transport by gravity waves, *Q. J. R. Meteorol. Soc.* **95**, 213 (1969).
  - [7] B. King, H. P. Zhang, and H. L. Swinney, Tidal flow over three-dimensional topography in a stratified fluid, *Phys. Fluids* **21**, 116601 (2009).

- [8] G. Bordes, A. Venaille, S. Joubaud, P. Odier, and T. Dauxois, Experimental observation of a strong mean flow induced by internal gravity waves, *Phys. Fluids* **24**, 086602 (2012).
- [9] N. Grisouard, M. Leclair, L. Gostiaux, and C. Staquet, Large scale energy transfer from an internal gravity wave reflecting on a simple slope, *Proc. IUTAM* **8**, 119 (2013).
- [10] B. Semin, G. Facchini, F. Pétrélis, and S. Fauve, Generation of a mean flow by an internal wave, *Phys. Fluids* **28**, 096601 (2016).
- [11] T. Dauxois, S. Joubaud, P. Odier, and A. Venaille, Instabilities of internal gravity wave beams, *Annu. Rev. Fluid Mech.* **50**, 131 (2018).
- [12] S. J. Lighthill, Acoustic streaming, *J. Sound Vib.* **61**, 391 (1978).
- [13] T. M. Rogers, D. N. C. Lin, and H. H. B. Lau, Internal gravity waves modulate the apparent misalignment of exoplanets around hot stars, *Astrophys. J.* **758**, L6 (2012).
- [14] R. S. Lindzen and J. R. Holton, A theory of the quasi-biennial oscillation, *J. Atmos. Sci.* **25**, 1095 (1968).
- [15] J. R. Holton and R. S. Lindzen, An updated theory for the quasi-biennial cycle of the tropical stratosphere, *J. Atmos. Sci.* **29**, 1076 (1972).
- [16] R. A. Plumb, The interaction of two internal waves with the mean flow: Implications for the theory of the quasi-biennial oscillation, *J. Atmos. Sci.* **34**, 1847 (1977).
- [17] R. A. Plumb and A. D. McEwan, The instability of a forced standing wave in a viscous stratified fluid: A laboratory analogue of the quasi biennial oscillation, *J. Atmos. Sci.* **35**, 1827 (1978).
- [18] B. Semin, N. Garroum, F. Pétrélis, and S. Fauve, Nonlinear Saturation of the Large Scale Flow in a Laboratory Model of the Quasibiennial Oscillation, *Phys. Rev. Lett.* **121**, 134502 (2018).
- [19] D. C. Fritts and H.-G. Chou, An investigation of the vertical wavenumber and frequency spectra of gravity wave motions in the lower stratosphere, *J. Atmos. Sci.* **44**, 3610 (1987).
- [20] L.-A. Couston, D. Lecoanet, B. Favier, and M. Le Bars, Order Out of Chaos: Slowly Reversing Mean Flows Emerge from Turbulently Generated Internal Waves, *Phys. Rev. Lett.* **120**, 244505 (2018).
- [21] P. Léard, D. Lecoanet, and M. Le Bars, Multimodal Excitation to Model the Quasibiennial Oscillation, *Phys. Rev. Lett.* **125**, 234501 (2020).
- [22] A. Renaud and A. Venaille, On the Holton-Lindzen-Plumb model for mean flow reversals in stratified fluids, *Q. J. R. Meteorol. Soc.* **146**, 2981 (2020).
- [23] D. Lecoanet, M. Le Bars, K. J. Burns, G. M. Vasil, B. P. Brown, E. Quataert, and J. S. Oishi, Numerical simulations of internal wave generation by convection in water, *Phys. Rev. E* **91**, 063016 (2015).
- [24] G. Oster, Density gradients, *Sci. Am.* **213**, 70 (1965).
- [25] W. D. Baines, Entrainment by a plume or jet at a density interface, *J. Fluid Mech.* **68**, 309 (1975).
- [26] P. Meunier and T. Leweke, Analysis and treatment of errors due to high velocity gradients in particle image velocimetry, *Exp. Fluids* **35**, 408 (2003).
- [27] H. Félouah and A. Pollard, The velocity spectra and turbulence length scale distributions in the near to intermediate regions of a round free turbulent jet, *Phys. Fluids* **21**, 115101 (2009).
- [28] D. Lecoanet and E. Quataert, Internal gravity wave excitation by turbulent convection, *Mon. Not. R. Astron. Soc.* **430**, 2363 (2013).
- [29] J. K. Ansong and B. R. Sutherland, Internal gravity waves generated by convective plumes, *J. Fluid Mech.* **648**, 405 (2010).
- [30] S. Boury, P. Odier, and T. Peacock, Axisymmetric internal wave transmission and resonant interference in nonlinear stratifications, *J. Fluid Mech.* **886**, A8 (2020).
- [31] K. J. Burns, G. M. Vasil, J. S. Oishi, D. Lecoanet, and B. P. Brown, Dedalus: A flexible framework for numerical simulations with spectral methods, *Phys. Rev. Research* **2**, 023068 (2020).
- [32] P. Léard, Etude de l'interaction entre écoulements turbulent et stratifié: convection pénétrante, ondes internes de gravité et écoulements grande échelle, PhD diss., Aix-Marseille Université, 2020.